International Journal of Sciences: Basic and Applied Research (IJSBAR)

ISSN 2307-4531
(Print & Online)

http://gssrr.org/index.php?journal=JournalOfBasicAndApplied

Purple Coloured Natural Ruby: X-ray Photoelectron Spectroscopy, X-ray Diffraction, X-ray Tomography and Other Microstructural Characterizations

Bijan Bihari Nayak[a], Tapan Dash[b*] and Barada Kanta Mishra[c]

[a,b,c] *CSIR-Institute of Minerals and Materials Technology, Bhubaneswar-751013, Odisha, India*

[a]*Email: bbnayak@immt.res.in*

[b]**Email: tapanphy@gmail.com*

[c]*Email: bkm@immt.res.in*

Abstract

Purple coloured natural ruby has been studied by surface sensitive tool like XPS supported by XRD, X-ray tomography (micro CT), FESEM, TEM and EDS. While XPS and EDS established the presence of transitional elements like Cr, Fe, Ti, the phases, morphologies and microstructures were studied by XRD, FESEM and TEM. X-ray micro CT provided non-destructive insights into the morpho-structural state of sample. UV-Vis and FTIR spectra of the ruby, recorded both in absorbance and reflectance mode, confirmed the occurrence of the above transitional elements contributing to typical colour display. Core level spectra of Cr, Fe, Ti, Al and O studied by XPS identified the ionic states of the elements. Results of the systematic and detailed investigations carried out in the study conclude that presence of low quantities (trace levels) of Cr, Fe,Ti coupled with inter-valence charge transfer between Fe and Ti accounts for the purple colour of natural ruby. The paper further highlights how surface and bulk characterization studies together facilitate better interpretation and meaningful conclusion.

---

*Corresponding author.

Keywords: Purple Coloured Ruby; XRD; XPS; X-ray Micro CT; Inter-Valence Charge Transfer; Microstructure; Ti^{3+}; Fe^{3+}; Cr^{3+}; UV-Vis Spectra.

1. Introduction

Ruby is a precious coloured gem where Cr-related light emission takes place in corundum (Al_2O_3). The thermo-mechanical properties of ruby are excellent and rival those of diamond [1]. Pure corundum appears white or colourless but presence of small amounts of transitional impurities such as Cr, Ti, Fe, V, Cu, Mg produces colour like red, pink, orange and several mixed shades [2-12]. Electronic transition taking place in ruby at the outer $3d^3$ shells of Cr^{3+} ions gives rise to red colour. Such mechanism is exploited to produce tunable laser and sensors for temperature and pressure. Despite several applications of ruby in current technologies, the aesthetic use of the gem overtakes all other uses because of its deep red colour (pigeon blood) and attractive shades. Ruby, particularly of natural origin, has been in use by mankind over many centuries, thus relatively common scientific techniques/methods like UV-Vis optical spectra [13, 14], X-ray diffraction (XRD) [15-17], IR (infrared), ESR (electron spin resonance) and Raman spectroscopy [9, 18-22] were the first to be applied and reported in literature for characterization and evaluation. In such a backdrop, few works on characterization of ruby by XPS (X-ray photoelectron spectroscopy) come to notice [16, 23] and that too any published work hardly exist today on X-ray micro computed tomography (micro CT) study of ruby.

XPS is a modern surface sensitive tool; however, for any unambiguous characterization / identification of material, its result has to be adequately backed by bulk microstructural analysis. In such scenario, important bulk characterization tools like XRD (X-ray diffraction), FESEM (field emission scanning electron microscopy), TEM (transmission electron microscopy), SAED (selected area electron diffraction), EDS (energy dispersive spectra of x-ray), UV-Vis (ultraviolet-visible) and FTIR (Fourier transform infrared) spectroscopy have been employed in this work to support and complement the XPS results. For the first time, latest non-destructive technique like X-ray micro CT has been used here to obtain direct visual picture of total internal structure and reconstruct three dimensional (3D) image of ruby. The overall study experimentally establishes the existence of Ti^{3+} jointly with Fe^{3+} and Cr^{3+} to account for the mixed colour / shade (purple) in the natural ruby.

Purple ruby of natural origin has been chosen in this work because of its easy and abundant availability in the vicinity. Its mixed shade is appealing from aesthetic standpoint. The experimental results in the investigation are loaded with potential scope for improvement of colour / shade of low grade rubies through use of several processing techniques (heat treatment, chemical leaching, plasma, laser, e-beam, ion implantation, etc.) towards high value addition. One may like to avail the scientific results of the study for artificial growth of purple ruby crystals (using crystal growth processes like Czochralski, Bridgman and Vernouli) towards commercial exploitation.

2. Materials and methods

The typical purple colour / shade exhibited by natural ruby (origin: Kalahandi, Odisha, India) used in this work

is shown in figure 1. The rubies shown in the figure are 0.5-1.5 cm in size. Some of them were pulverized to -300 BSS (53 μm) size for various characterization studies. While powder samples were employed for XPS, XRD, TEM, SAED and FTIR, polished specimens were used for FESEM, EDS and UV-Vis spectrometry studies. X-ray photoelectrons were collected from pelletized powder sample by employing the model S/N-10001 (Project No. 251, Prevac, Poland) with a VG Scienta-R3000 hemispherical energy analyzer. AlK_{α} radiation (operating at 200 W, 10 kV and 20 mA) was employed as the incident radiation and ultra high vacuum condition ($>10^{-9}$ mbar) was maintained in the chamber during analysis. General resolution of the instrument: 0.2 eV. The spectrometer was well calibrated taking Ag standard and referring to the B.E. of the $Ag3d_{5/2}$ (368.2 eV). While Full survey spectra (0-1486.0) were recorded at pass energy 200 eV, high-resolution spectra (at specific peaks) were recorded at 20 eV pass energy. XRD pattern of powder sample was recorded in 2θ range $6\text{-}100^0$ by employing PANalytical X'Pert Pro diffractometer using CuKα radiation (λ = 0.15406 nm). Noting the observed peak positions, *d* values were determined and *hkl* indices of planes were assigned by comparison with the *d* values in JCPDS (1999) data files (Table 1). Surface morphologies of the polished samples were observed under FESEM (ZEISS SUPRA 55). Microstructures of the grains were observed by TEM: TECNAI G^2 (200 kV), FEI, Netherland having additional facility for selected area electron diffraction (SAED). The Gatan Inc.'s digital micrograph™ software was used to identify the phases and their corresponding planes from SAED pattern. Elemental compositions were studied by EDS attached both to FESEM and TEM. Internal and external (surface) imaging and microstructural investigation of the ruby sample was performed by an X-ray micro CT (model: SkyScan 2211, Bruker, Belgium). The best achievable spatial resolution of the CT machine is 600 nm. Reconstruction of scanned images was performed by using SkyScan's InstaRecon software. Sample was scanned with a full 360^0 rotation (0.2^0 increments) at following conditions: accelerating voltage - 60 kV and target current- 270 μA. The reconstructed images were transferred into 3D models using CTvox and Avizo 9.0.0 platforms. FTIR spectra for powder samples were recorded in the range 400-4000 cm^{-1} using a Perkin-Elmer Spectrum GX spectrometer with spectral resolution of 1 cm^{-1}. All the characterization facilities are available at the CSIR-Institute of Minerals and Materials Technology (CSIR-IMMT), Bhubaneswar, India.

3. Results

3.1 XPS studies

XPS of the ruby samples was studied using AlK_{α} radiation and the broad spectral feature (full survey spectra) of a typical sample is shown in figure 2a. The binding energy (BE) spectra show the presence of several elements. The de-convoluted (following Gaussian-Lorentzian curve fitted function) high resolution core level spectra of Cr2p, Al2p, Ti2p, Fe2p and O1s states are shown in figure 2b, figure 2c, figure 2d, figure 2e and figure 2f respectively. The Cr2p spectra when de-convoluted (figure 2b) produce two peaks respectively at 576.7 and 586.6 eV due to Cr^{3+}. The core level BE spectra of Al 2p shown in figure 2c when de-convoluted produce two peaks at 74.1 and 75.3 eV respectively due to Al^{3+} and mixed valence states . The de-convolution of Ti 2p spectra produce four peaks (figure 2d). The signatures due to Ti^{3+} (457.6 eV:$2p_{3/2}$, 463.5 eV:2 $p_{1/2}$) and Ti^{4+} (458.5 eV:$2p_{3/2}$, 464.7 eV:2 $p_{1/2}$) are identified here. The spectra of Fe 2p shown in figure 2e when de-convoluted produce four peaks. While two of the peaks show signatures of Fe^{2+} at BE of 708.5 and 722.4 eV, the rest two peaks at 710.6 and 724.4 eV are the signatures of Fe^{3+}. The O1s spectra (figure 2f) show three different peaks at

530, 531.7 and 534.3 eV upon de-convolution. These peaks are the signatures of three different oxygen species, which may be ascribed to lattice site / surface oxygen contamination. The summary of all XPS results including possible peak assignments is presented in Table 2.

Figure 1: Typical purple colour / shade of the natural ruby used in the study.

Table 1: JCPDS (1999) data files used for identifying various phases (with space groups) in the ruby sample and their lattice constant values.

Phase and Structure	Lattice constants (in nm)			Space group	JCPDS (1999)
	a	*b*	*C*		
Al_2O_3 (Rhombohedral)	0.47588		1.2992	$R\bar{3}c$ (167)	42-1468
$Al_2O_3.3H_2O$ (Monoclinic)	0.8624	0.5060	0.9700	$P2_1/n$(14)	02-0249
$Al_2O_{3.54}SiO_2$ (Orthorhombic)	2.0104	1.9897	1.3395	Pnma (62)	44-0003
Cr_2O_3 (Rhombohedral)	0.49516		1.35987	$R\bar{3}c$ (167)	84-1616
TiO_2 (Tetragonal)	0.4508		0.3027	P42/mnm (136)	82-0514

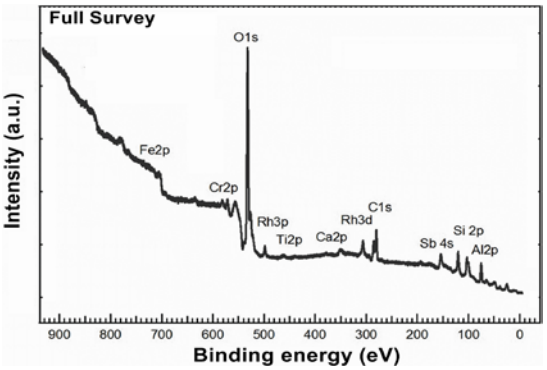

Figure 2a: Full survey XPS spectra of the purple ruby.

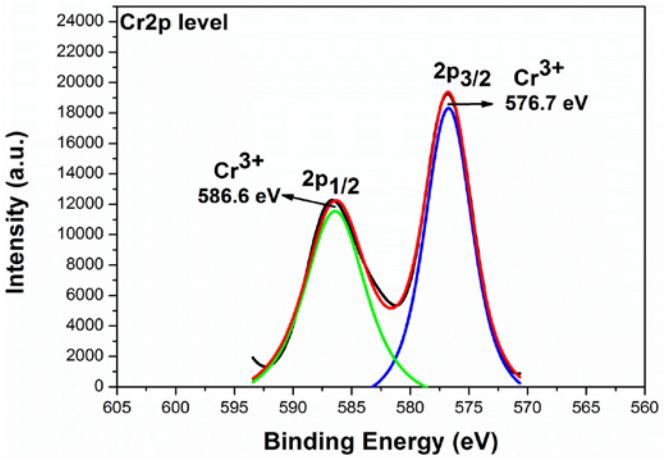

Figure 2b: XPS spectra of Cr2p level in the purple ruby.

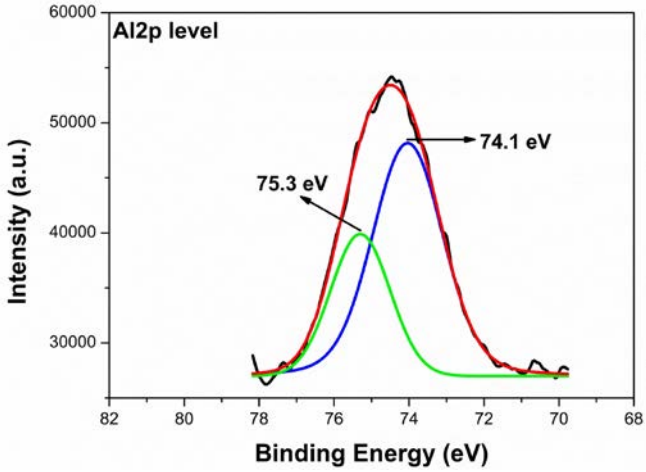

Figure 2c: XPS spectra of Al2p level in the purple ruby.

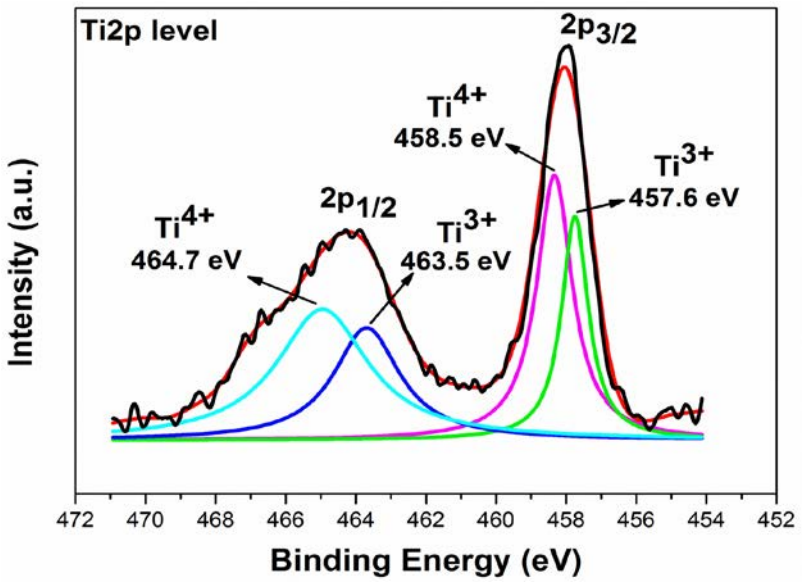

Figure 2d: XPS spectra of Ti2p level in the purple ruby.

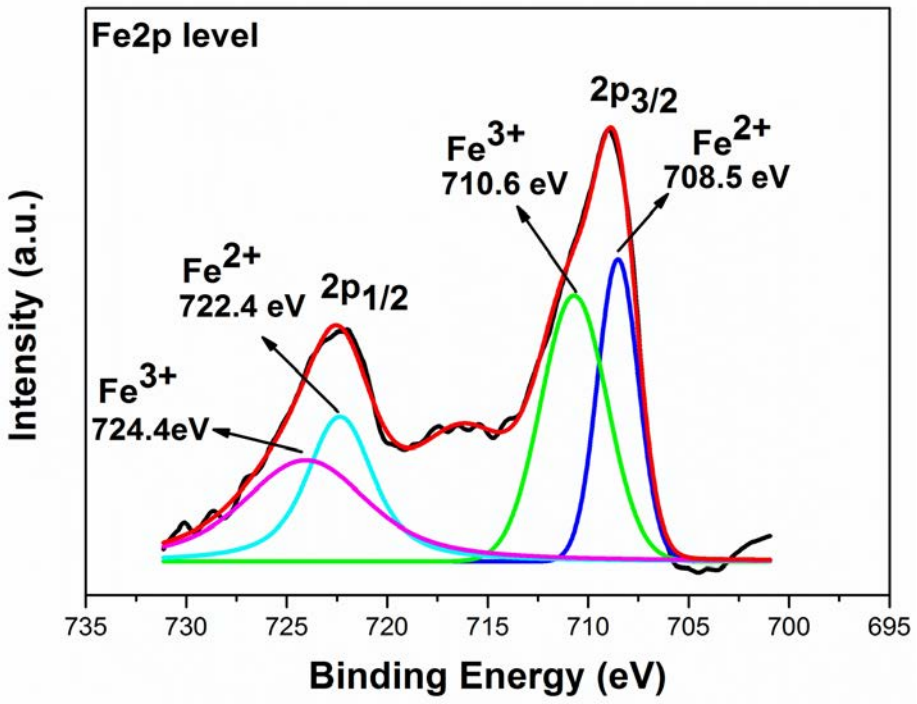

Figure 2e: XPS spectra of Fe2p level in the purple ruby.

3.2 XRD and SAED studies

Figure 3 shows the XRD pattern observed for the purple ruby. By determining the *d* values and comparing them with JCPDS data files (Table 1), identification of crystallographic phases was done. Major phases thus identified and their possible planar indices (*hkl*) are shown in Table 3. Al_2O_3 (including water of crystallization) is found to

be the major phase; Cr_2O_3, TiO_2 and $Al_2O_3{\cdot}_{54}SiO_2$ are noticd to be the minor phases (corresponding to smaller peaks). All the phases except aluminium silicate are detected in the selected area electron diffraction (SAED) pattern shown in figure 4. Table 4 presents the determined *d* values, identified phases and correspong planes (*hkl*) observed from SAED pattern.

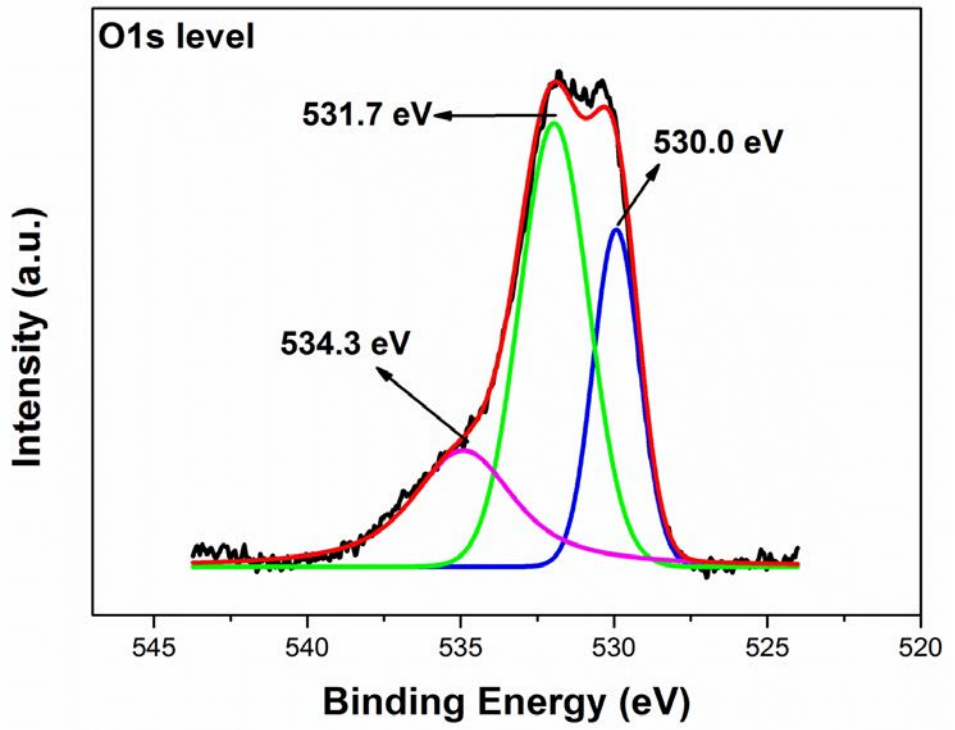

Figure 2f: XPS spectra of O1s level in the purple ruby.

3.3 FESEM, TEM and EDS studies

Figure 5a shows the surface microstructure of a typical purple ruby (as-collected and polished) by FESEM. Figure 5b shows EDS of elements detected at a point located on a selected grain, as indicated spectrum 1 in figure 5a. EDS recorded at a point just outside the selected grain (indicated as spectrum 2 in figure 5a) is shown in 5c. The EDS peak intensities of Al, Ti, Si, O and trace elements are observed to vary across the sample surface. TEM microstructures of the purple ruby (observed at two different points) are shown in figure 6a and 6b and their corresponding EDS are presented in figure 6c and 6d respectively. Very small peaks of Cr and Fe are marked in the energy range of 5.1- 6.1 and 6.1-7.1 keV respectively and their distributions also are found to vary across the surface.

3.4 X-ray micro CT studies

Figure 7(a-e) shows the external (surface) and internal (morpho-structure) images recorded for the ruby sample by employing the non-destructive radiation technique such as X-ray micro CT. Specimen was used in its natural form (no processing or preparation like thin sectioning, surface polishing, etc. was done). While surface tomographic image is shown in figure 7(a), figure 7(b) shows the internal tomographic morphology (all in grey

scale). Figure 8 shows the internal structure of the specimen in grey scale being transferred to colour form (given virtual colours). Figure 7c, d and e show the grey images of slices through the center of the sample which are taken in X-Y, Y-Z and Z-X planes of the CT scanner's co-ordinate system. Several mineral phases (inclusions / impurities) along with matrix are noticed in figure 7 and 8.

Table 2: Binding energy (BE) values of Cr2p, Al2p, Ti2p, Fe 2p and O1s levels determined from XPS analysis of the purple ruby.

Core level spectra		BE (eV) values and peak assignment in the observed core level spectra		
Cr2p level	$Cr2p_{3/2}$	576.7 Cr^{3+} (Cr_2O_3)		
	$Cr2p_{1/2}$	586.6 Cr^{3+} (Cr_2O_3)		
Al2p level		74.1 Al^{3+} (Al_2O_3)	75.3 Al-O-H such as AlO(OH), $AlO(OH)_2$, $Al(OH)_3$	
Ti2p level	$Ti2p_{3/2}$	457.6 Ti^{3+} (Ti_2O_3)	458.5 Ti^{4+} (TiO_2)	
	$Ti2p_{1/2}$	463.5 Ti^{3+} (Ti_2O_3)	464.7 Ti^{4+} (TiO_2)	
Fe2p level	$Fe2p_{3/2}$	708.5 Fe^{2+} (FeO)	710.6 Fe^{3+} (Fe_2O_3, α-FeOOH)	
	$Fe2p_{1/2}$	722.4 Fe^{2+} (FeO)	724.4 Fe^{3+} (Fe_2O_3, α-FeOOH)	
O1s level		530.0 (O^{2-}) Cr_2O_3, FeO, FeOOH, TiO_2	531.7 Al_2O_3, $Al_2O_3.3H_2O$, AlO(OH)	534.3 Surface contaminated OH

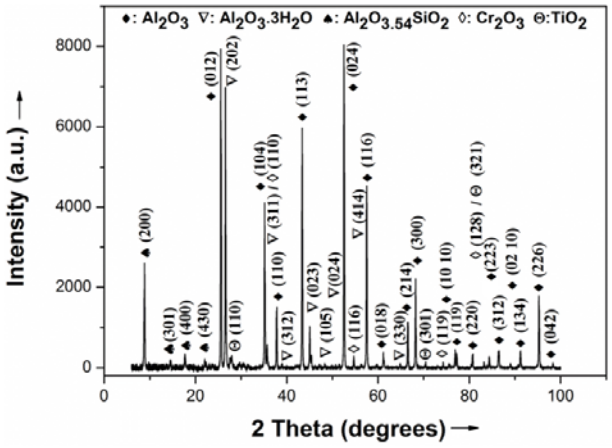

Figure 3: XRD pattern of the purple ruby showing presence of various phases.

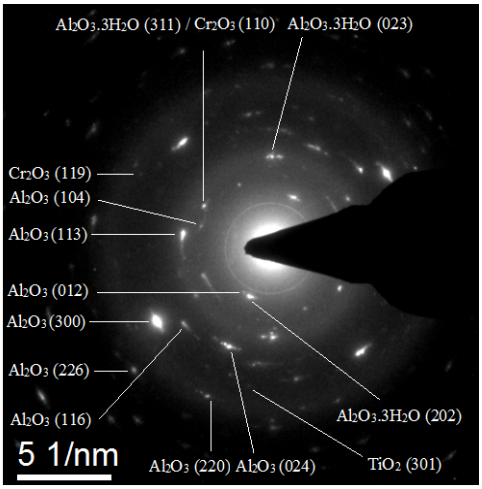

Figure 4: SAED pattern of the purple ruby.

Table 3: Major crystallographic phases (identified from strong peaks in XRD) and corresponding planes in the purple ruby sample.

d-spacing (nm) determined from XRD	*d*-spacing (nm) and corresponding phases in JCPDS data files (Table 1)	Planes identified (*hkl*)
1.001301	1.00201, $Al_2O_{3.54}SiO_2$	(200)
0.348268	0.348, Al_2O_3	(012)
0.335022	0.333, $Al_2O_3.3H_2O$	(202)
0.255201	0.2551, Al_2O_3	(104)
0.237892	0.2379, Al_2O_3	(110)

0.208434	0.2085, Al_2O_3	(113)
0.200738	0.199, $Al_2O_3.3H_2O$	(023)
0.173971	0.17398, Al_2O_3	(024)
0.160106	0.16014, Al_2O_3	(116)
0.140424	0.14045, Al_2O_3	(214)
0.137346	0.13738, Al_2O_3	(300)
0.104253	0.10427, Al_2O_3	(226)

3.5 UV-Vis spectral studies

Reflectance and absorbance spectra of polished purple ruby specimen were recorded in the UV-visible region and the results are presented in figure 9. The reflectance is seen to rise from 425 to 480 nm, followed by an inflexion. Relatively sharp rise is noticed to take place at 450-470 nm. Another rise at 580 nm is also observed which continues till a very steep rise takes place between 590 and 650 nm. It may be mentioned that 425 nm and 590 nm are the onset wavelengths of blue and pink colours respectively. The absorbance spectra in the figure are found to be opposite in nature to the reflectance spectra.

3.6 FTIR spectral studies

FTIR spectra (absorbance as well as reflectance) recorded for the purple ruby (taken in pelletized powder form) is shown in figure 10. The absorbance intensities in the plot have been multiplied 120 times to strengthen the peaks for a suitable comparison with the reflectance spectra. The nature of the reflectance spectra in the figure is seen to be almost opposite to the absorbance spectra, a finding similar to that observed in figure 9.

Table 4: Crystallographic phases with corresponding planes identified from SAED pattern of the purple ruby (using Gatan Inc.'s digital micrograph^{TM} software).

d-spacing (nm) determined from SAED	Phases and planes (*hkl*) identified
0.34616	Al_2O_3 (012)
0.33404	$Al_2O_3.3H_2O$ (202)
0.25540	Al_2O_3 (104)
0.25046	$Al_2O_3.3H_2O$ (311) / Cr_2O_3 (110)
0.20954	Al_2O_3 (113)
0.19974	$Al_2O_3.3H_2O$ (023)

0.17086	Al_2O_3 (024)
0.16221	Al_2O_3 (116)
0.13446	Al_2O_3 (300)
0.133672	TiO_2 (301)
0.12654	Cr_2O_3 (119)
0.11676	Al_2O_3 (220)
0.10527	Al_2O_3 (226)

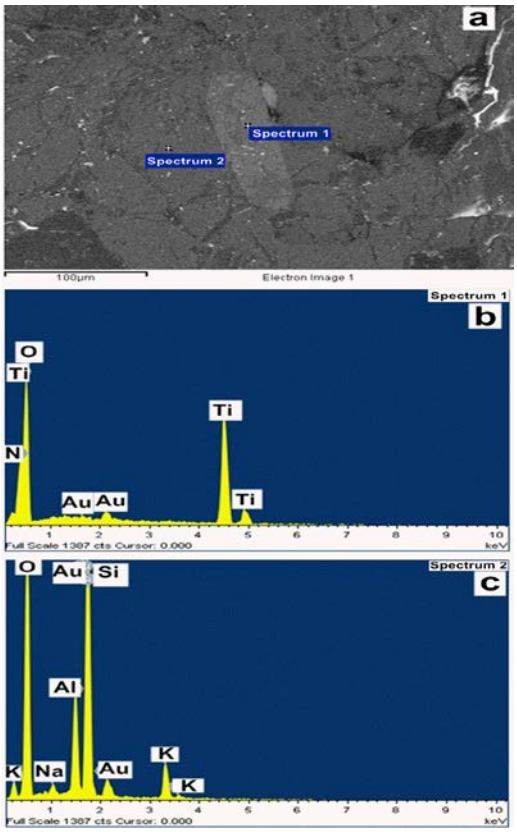

Figure 5: (a) FESEM image of the purple ruby

(b) Corresponding EDS observed at a point on a selected grain, indicated as spectrum 1 in (a)

(c) Corresponding EDS observed at a different point (outside the typical grain), indicated as spectrum 2 in (a).

4. Discussion

XPS is a highly surface sensitive tool. With the present spectrometer, a depth maximum up to 10 nm could be analysed. Since colour / shade of ruby is influenced by factors like refractive index, absorption coefficient, etc., it is necessary to do the bulk characterizations before XPS study. The discussion here therefore prefers first to address the results obtained from XRD, SAED, FESEM, TEM, X-ray micro CT and EDS. UV-Vis and FTIR studies.

From the XRD pattern shown in figure 3, the *d* values were determined and the possible phases and *hkl* indices of the planes have been identified by comparing with JCPDS data files (Table 1). It is observed that the peaks / reflections are mostly due to alumina and its associated phases: Al_2O_3, $Al_2O_3.3H_2O$ and $Al_2O_3{}_{.54}SiO_2$. The results are summarized in Table 3. It is evident that while Al_2O_3 shows two strong peaks, three medium intensity peaks, three weak peaks and seven very weak peaks, its phase containing water of crystallization ($Al_2O_3.3H_2O$) exhibits one strong peak, one weak peak and three very weak peaks.

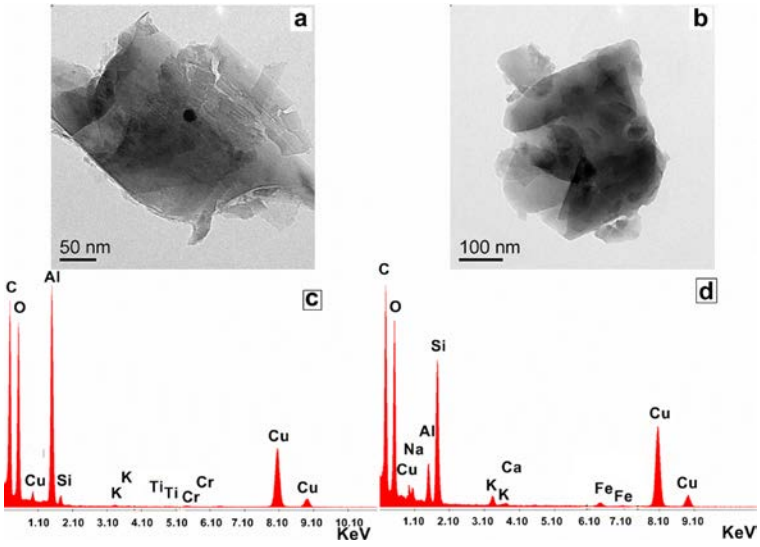

Figure 6: (a) TEM microstructure of the purple ruby (b) TEM microstructure of the same ruby recorded at a different point (c) EDS corresponding to figure (a) showing presence of Cr (d) EDS corresponding to figure (b) showing presence of Fe.

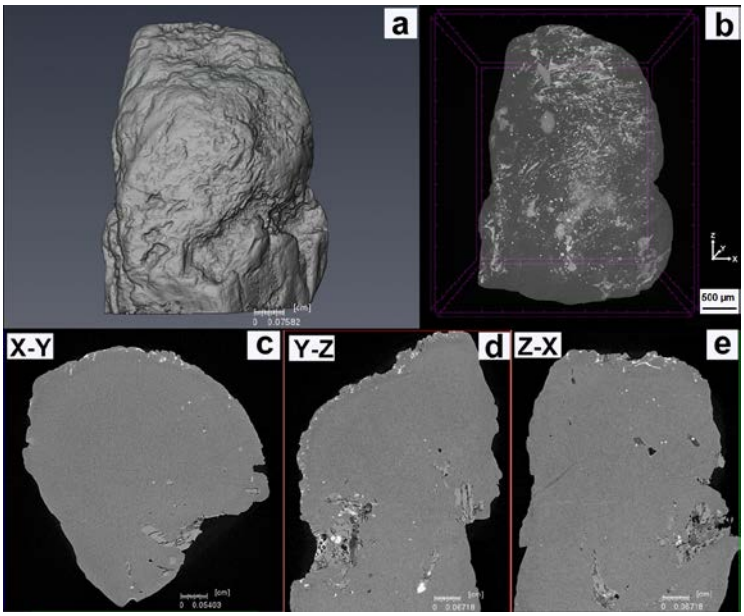

Figure 7: Sequence of grey images of the purple ruby recorded by X-ray micro CT: (a) surface tomographic image (b) internal tomographic image; (c), (d) and (e) images of tomographic slices through center of specimen.

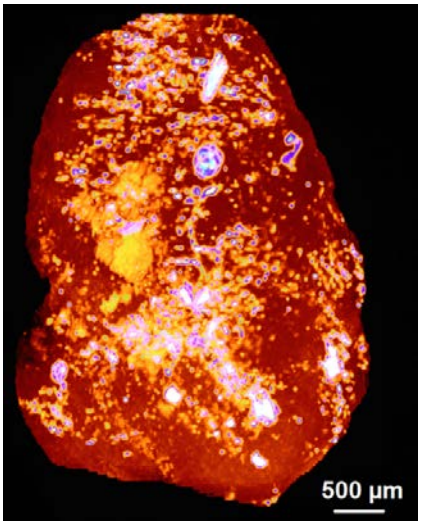

Figure 8: Transferred colour (virtual colour) tomographic image of figure7 (b) showing internal structure of the ruby: matrix-dark red, impurities-yellow, white and dark blue.

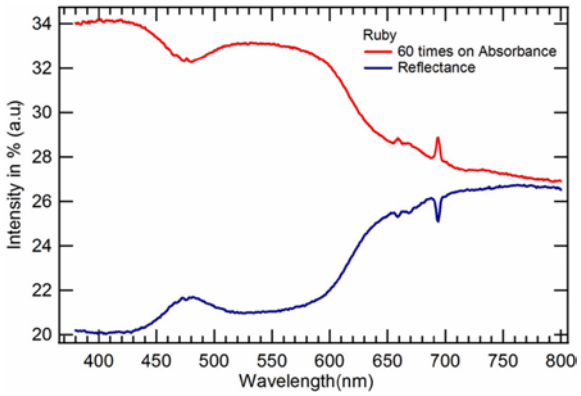

Figure 9: UV-Vis absorbance and reflectance spectra of the purple ruby.

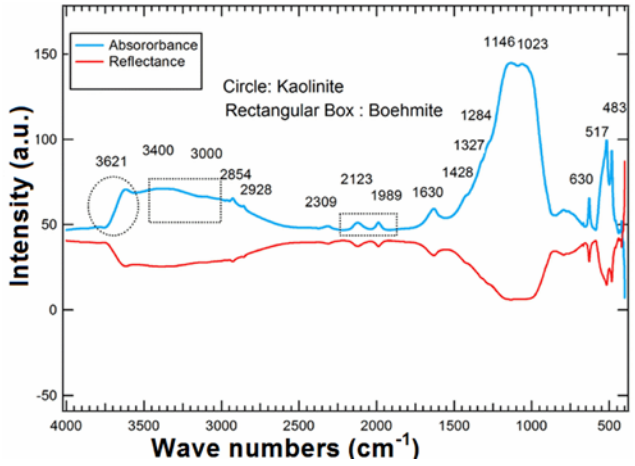

Figure 10: FTIR absorbance and reflectance spectra of purple ruby.

Aluminium silicate ($Al_2O_3.{}_{54}SiO_2$) shows one medium intensity peak and three weak peaks. Further, the XRD pattern exhibits two weak peaks due to Cr_2O_3 and two weak peaks due to TiO_2. Such poor intensity peaks are quite expected due to their low contents in the ruby. It may be interesting to note the considerable presence of water of crystallization ($3H_2O$) in alumina. Such acquiring of water molecule in ruby appears unusual because aluminium hydrate ($Al_2O_3.3H_2O$ / $Al(OH)_3$) is known to be produced (Bayer's process) when alumina is treated with the solution of NaOH at 175^0 C under pressure to produce $NaAlO_2$ (alkaline solution), followed by cooling under bubbling CO_2 [24]. Since the ruby used here is of natural origin, Bayer's route of formation of $Al_2O_3.3H_2O$ appears to be far-fetched. It might have taken place under the earth crust by natural processes. Hydroxylated alumina ($Al(OH)_3$) exists in two major forms: diaspore and bohemite [25]. The presence of diaspore in ruby has been detected by some workers using IR spectroscopic data, as can be found in literature [26-28]. The present study in contrast detects $Al_2O_3.3H_2O$ / $Al(OH)_3$ from XRD.

The SAED pattern shown in figure 4 has been identified and summarized in Table 4. Except aluminium silicate ($Al_2O_3.{}_{54}SiO_2$), the rest of the phases observed in XRD are detected in SAED. The *d* values and their corresponding *hkl* indices are presented in the Table 3. The FESEM microstructure (figure 5a) of the typical ruby sample shows polycrystalline morphology on the surface. Single crystal ruby is produced by nucleation and controlled growth process where directional withdrawal of heat/cooling takes place very slowly, e.g. Czochralski method. Since the origin of the ruby investigated here is mine/earth crust, one can hardly expect the above controlled process conditions to have existed in the earth crust at the time of crystal formation millions of year ago. figure 5b and 5c (EDS) show the presence of elements such as Al, Ti, Si, O. Cr is not detected in such micron level scanning. Strong peak due to Au is seen to arise from gold coating of specimen in FESEM scanning. Since Cr is the most crucial impurity element in ruby that produces red colour, it becomes quite pertinent to ascertain its presence. The ruby sample was therefore taken in the form of fine powder to do TEM study. The powder was ultrasonicated in ethanol medium, and then one drop of the suspension liquid was loaded on to copper grid (carbon coated) of 2 mm diameter followed by drying under IR lamp. The grid was introduced into the TEM and the microstructure of the fine ruby grain along with EDS of the sample was observed. The results are presented in figure 6. From the nm scale microstructures shown in figure 6a and 6b, more refined morphologies are seen. Corresponding EDS shown in figure 6c and 6d respectively show the presence of various elements in the ruby matrix. While figure 6c detects Al, Si, Ti, Cr and O, figure 6d records Al, Si, Fe and O. X-ray micro CT images presented in figure 7 (a, c, d, e) show the grey images of top surface as well as three slices through centre of specimen. Internal characteristic and morpho-structural investigation of ruby sample. Irregular undulations noticed on the surface of ruby (figure 7a) may be attributed to its genesis from mine/earth crust. The 3-D tomographic grey scale image shown in figure 7b was transferred to colour image (figure 8) for easy distinction between different phases present in the sample by assigning different colours to them. Four types of phases are marked by different colour codes: matrix (deep red), impurities/inclusions (yellow, white and dark blue). The presence of at least four types of phases is also evident from tomographic slices shown in figure 7 c, d, & e: matrix (grey) and impurities (light grey, deep grey and white). Some micro cracks are observed in figure 7d & e. Consolidating the FESEM, TEM and X-ray micro CT results one may find that impurities distributions are not uniform in the ruby at sub-micron / nm levels.

UV-Vis spectra of the ruby are presented in figure 9. It is marked that the rise in reflectance occurs at 425 and

580 nm respectively. Since 425 and 590 nm are the onset wavelengths of blue and pink colours respectively, the above two rises may be due to the presence of Ti and Cr. Thirangoon [29] has reported that optical absorption at around 426 and 540 nm occurs due to Ti^{4+} and Cr^{3+} respectively and the absorption at around 470 nm occurs due to Fe^{3+}. The UV-Vis absorption spectra studied on diaspore samples of Turkey show similar results [30, 31]. In the present case, the occurrence of strong absorption (figure 9) at around 470 nm may therefore be attributed to Fe^{3+}.

The FTIR spectra (absorbance and reflectance) of the ruby (figure 10) have been interpreted based on literature report [29]. Accordingly, the absorption peak at 3621 cm^{-1} (marked as circle) may be attributed to kaolinite ($Al_2 Si_2 O_5 (OH)_4$). Boehmite (γ-AlO(OH)) is ascribed to the peaks at 1989 cm^{-1}, 2123 cm^{-1} and to the broad absorption band in the range 3000-3400 cm^{-1} (indicated with two rectangular boxes). Following Schwarz et al. [32] in case of ruby of Tanzania origin, one may assign the peaks at 1989, 2123, 2928 and 3000 cm^{-1} to diaspore (due to structurally bound-OH bond). The FTIR results are seen to corroborate our XRD results.

XPS survey spectra and the de-convoluted peaks of the core level high resolution spectra for various elements in the ruby sample are presented in figure 2 (a-f). Table 2 summarizes all the results of the XPS analysis. To begin with, one can always look for the core level spectra of Al because the basic matrix of ruby is alumina. As seen from figure 2c and Table 2, the single peak arising due to Al2p (in the survey spectra) produces two separate peaks at 74.1 and 75.3 eV respectively after de-convolution. Following literature [33], the first peak (strong) is assigned to Al^{3+}, as in the case of Al_2O_3 and the second peak (weak) may be attributed to Al but the valence state may be 1^+, 3^+ , etc. as in the case of AlO(OH), $Al(OH)_3$ and $AlO(OH)_2$ (see Table 2). In view of the evidence obtained for $Al(OH)_3$ from XRD and the evidence for boehmite (γ-AlO(OH)) obtained from FTIR (as reported above), one may think of a mixed valency state for Al to exist in the present case of purple ruby.

Figure 2b shows well-defined spin-coupled peaks at the BE of 576.7 eV and 586.6 eV for $Cr2p_{3/2}$ and $Cr2p_1/2$ respectively. As per literature [34-36], the $Cr2p_{3/2}$ and $Cr2p_{1/2}$ peaks are attributed to Cr^{3+}. Figure 2d depicts the de-convoluted spectra of Ti2p. It may be observed from Table 2, the peaks attributed to Ti^{3+} are at 457.6 eV ($Ti2p_{3/2}$) and 463.5 eV ($Ti2p_{1/2}$); the peaks at 458.5 eV ($Ti2p_{3/2}$) and 464.7 eV ($Ti2p_{1/2}$) are attributed to Ti^{4+} [37-39]. Similarly, figure 2e and Table 2 show that the peaks at 708.5 eV ($Fe2p_{3/2}$) and 722.4 eV ($Fe2p_{1/2}$) are attributed to Fe^{2+}; the peaks at 710.6 eV ($Fe2p_{3/2}$) and 724.4 eV ($Fe2p_{1/2}$) are due to Fe^{3+} [23, 40, 41]. The O1s level spectra (figure 2f) is observed at three energy levels (peaks), as shown in Table 2: 530.0, 531.7 and 534.3 eV and the ionic states of O are seen here to be similar to that exist in the compounds referred in Table 2 [36, 42, 43]. It is interesting to note that the O1s spectra corroborate the Al2p spectral finding in respect of Al_2O_3, AlO(OH) and $Al_2O_3.3H_2O/Al(OH)_3$. Similarly, the spectra corroborate the occurrence of both $Fe^{2+}$and Fe^{3+} (Fe-OOH, FeO) in the Fe2p spectra, and also corroborate the occurrence of Ti^{4+} (TiO_2) in the Ti2p spectra and Cr^{3+} (Cr_2O_3) in the Cr2p spectra. The O1s spectra further demonstrate that the surface of the purple ruby contains -OH whose origin is attributed in literature to contamination [42].

In the light of the above narratives, the salient findings in this investigation may be summarized as follows:

(i) XRD pattern shows the following peaks/reflections (corresponding to phases): Al_2O_3 (major), $Al_2O_3.3H_2O$ /

$Al(OH)_3$ (second major), $Al_2O_{3.54}SiO_2$ (medium); Cr_2O_3 (minor), TiO_2 (minor)

(ii) SAED pattern detects the following phases: Al_2O_3 (major), $Al_2O_3.3H_2O$ (second major), Cr_2O_3 (minor), TiO_2 (minor)

(iii) Morphology observed under FESEM & TEM: polycrystalline

(iv) X-ray micro CT (non-destructive testing) image of surface and interior: shows internal impurity inclusions

(v) Detection of elements:

(a) from EDS attached to FESEM: Al, Ti, Si, O

(b) from EDS attached to TEM: Al, Si, Ti, Cr, Fe, O

(vi) Transitional element ions detected by XPS:

Cr^{3+}, Ti^{3+}, Ti^{4+}, Fe^{2+}, Fe^{3+}

(vii) Ions identified in UV-Vis spectra: Cr^{3+}, Ti^{4+}, Fe^{3+}

It may be inferred from the above that XPS detect the presence of two additional ions in the purple ruby: Ti^{3+} and Fe^{2+}. Achiwawanich et al. [23] have discussed in the case of surface analysis of Mong Hsu rubies of Myanmar (Burma) that blue colour arises in ruby by Fe^{2+}/Ti^{4+} inter-valence charge transfer (IVCT). This can occur when the pair of Fe^{2+}/Ti^{4+} ions (within 0.01%) remain in adjacent positions in the Al_2O_3 matrix, allowing the overlap of their 3d orbitals [44, 45]. Our XPS spectra (figure 2e, Table 2) show the presence of Fe^{3+} and Fe^{2+} in the ruby in almost equal proportions. In ruby Fe^{3+} produces characteristic yellow colour and Cr^{3+} produces red colour (in octahedral environment in α-Al_2O_3) [8, 46]. A combined presence of Fe^{3+} and Cr^{3+} causes superposition of yellow and red that leads to produce colours like pink (with minimal traces of Cr & Fe) and orange (with higher concentration of Fe than Cr) [23, 47, 48]. Nassau [3] and other workers [26-28] have reported and discussed the issue of Fe and Ti in literature. According to Nassau [3], in sapphire and a variety of corundum, Al_2O_3, impurities like Fe and Ti can exist in two valence states with two combinations: (a) Fe^{2+} and Ti^{4+} (b) Fe^{3+} and Ti^{3+}. A single electron can be caused to transfer from the Fe to the Ti by light absorption and back again. Since state (b) has a higher energy than state (a), the transition from (a) to (b) involves the absorption of energy, producing a broad intense absorption band at the red end of the spectrum and resulting in the deep blue colour. Thus, in IVCT a light induced reversible reaction $Fe^{2+} + Ti^{4+} \leftrightarrow Fe^{3+} + Ti^{3+}$ takes place between state (a) and state (b).

As stated above, in ruby red colour is produced by small amount Cr^{3+} and blue colour is produced by trace amounts of Fe, Ti by IVCT mechanism. The superposition of red and blue colour produces the secondary colour magenta which is nothing but red purple. The colour of the natural ruby sample chosen in this investigation (figure 1) matches with red purple or magenta. The levels of Cr, Fe and Ti present in the ruby are marked to be

very low or traces, as seen from XPS (figure 2a) and EDS (figure 6c, 6d). Hence, the purple colour or hue of the typical ruby (in this study) is attributed to the presence of low quantities of impurities like Cr, Fe and Ti coupled with occurrence of light induced electron transfer between Fe and Ti.

5. Conclusion

In this study, a combined characterization approach involving latest surface and bulk techniques provides an accurate way to reason out the purple colour of natural ruby obtained from Kalahandi district of Odisha, India. While XPS focused on the detection of various transitional element ions in surface region, bulk techniques such as XRD, X-ray micro CT, FESEM, TEM, EDS, UV-Vis and FTIR provided a wide range of microstructural, tomographic and spectroscopic data to probe for the cause behind the secondary /mixed colour or hue. The study concludes that occurrence of low levels (trace amounts) of critical transitional elements such as Cr, Fe and Ti is basically responsible for the display of purple colour. Cr^{3+} produces red colour in the octahedral environment of α-Al_2O_3 and the light induced reversible reaction $Fe^{2+} + Ti^{4+} \leftrightarrow Fe^{3+} + Ti^{3+}$ causes IVCT producing blue colour. Superposition of these two colours (red and blue) thus produces magenta or red purple hue in ruby. Brilliant red or pigeon blood coloured ruby fetches highest price in market. The present study gives a clue as to how one can upgrade the purple ruby to more demanding red ruby. The objective could be achieved if intensity of blue emission is reduced in ruby by reduction of Ti and Fe levels adopting impurity removal methods like heat treatment, chemical leaching, plasma, laser heating, etc.

Acknowledgement

This work has been supported by the Council for Scientific and Industrial Research (CSIR Project No. ESC-206).

References

[1] L.C. Cossolino and A.R. Zanatta. “Influence of Chromium Concentration on the Optical-Electronic Properties of Ruby Microstructures.” J. Phys. D: Appl. Phys., vol. 43, pp. 015302 - 015310, 2010.

[2] L.E. Orgel. “Ion Compression and the Colour of Ruby.” Nature, vol. 179, p. 1348, 1957.

[3] K. Nassau. “The Origins of Color in Minerals.” Am. Miner., vol. 63, pp. 219-229, 1978.

[4] T.S. Bessonova, M.P. Stanislavskii, V.Ya. Khaimov-Mal’kov and A.I. Sobko. “Influence of Impurities on Radiation-Induced Optical Process in Ruby” J. Appl. Spectrosc., vol. 30, pp. 589-594, 1979.

[5] K. Nassau. Gemstone Enhancement, 2nd ed., Oxford, UK: Butterworth-Heinmann, 1984.

[6] P. Parikh, D.M. Bharadwaj, R.P. Gupta, N.L. Saini, S. Fernandes, R.K. Singhal, D.C. Jain, and K.B. Garg. “Comparative Study of the Electronic Structure of Natural and Synthetic Rubies using XAFS and EDAX Analyses.” Bull. Mater. Sci., vol. 25, pp. 653-656, 2002.

[7] K. Nassau. The Science of Color, 2nd ed., S.K. Shevell, Ed., Amsterdam: Elsevier Science Ltd., 2003, pp. 247-280.

[8] J.M. Garcia-Lastra, M.T. Barriuso, J.A. Aramburu and M. Moreno. "Origin of the Different Colour of Ruby and Emerald" Phys. Rev. B, vol. 72, pp. 113104:(1-4), 2005.

[9] A.S. Majumdar and G. Mathew. "Distinct Ruby Suite at Sardapur, Orissa: A spectroscopic Investigation." J. Geol. Soc. India, vol. 80, pp. 715-722, 2012.

[10] V. Pardieu, N. Rakotosaona, M. Noverraj and L.P. Bryl. "Ruby and Sapphire Rush Near Didy, Madagascar, Gems & Gemology." Gems. Gemol., vol. 48, pp. 149-150, 2012.

[11] "The Colors of Minerals.", Internet: http://minerals.gps.caltech.edu/color_causes/, 2014 [Dec.20, 2015].

[12] A.R. West. "Phase Diagrams of Inorganic Materials: Applications to Complex Solid-Solution Systems, Site Substitutions and Stoichiometry-Property Correlations." J. Mater. Chem., vol.3, pp. 433-440, 1993.

[13] D.S. McClure. "Comparison of the Crystal Fields and Optical Spectra of Cr_2O_3 and Ruby."J. Chem. Phys., vol. 5, pp. 38-39, 1963.

[14] B. Henderson. "Spectroscopic measurements" in Hand Book of Optics, 2nd ed, Vol. II, M. Bass, E.W.V. Stryland, D.R. Williams and W.L. Wolfe, Ed., McGraw-Hill, INC., 1995, pp. 20.

[15] V.G. Tsirelson, My. Antipin, R.G. Gerr, R.P. Ozerov and Yu.T. Struchkov, "Ruby Structure Peculiarities Derived from X-ray Diffraction Data Localization of Chromium Atoms and Electron Deformation Density."Phys. Stat. Sol., vol. 87, pp. 425-433, 1985.

[16] W. Li, Z.J. Coppens, G.D. Walker and J.G. Valentine. "Electron Beam Physical Vapour Deposition of Thin Ruby Films for Remote Temperature Sensing."J. Appl. Phys., vol. 113, p. 163509, 2013, http://dx.doi.org/10.1063/1.4802628.

[17] V. Hurai, M. Wierzbicka-Wieczorek, M. Pentrak, M. Huraiva, R. Thomas, A. Swierczewska and J. Luptakova. "X-ray Diffraction and Vibrational Spectroscopic Characteristic of Hydroxylclinohumite from Ruby Bearing Marbles (Luc Yen district, Vietnam." Int. J. Miner., article ID 648530, 11 pages, 2014, http://dx.doi.org/10.1155/2014/648530.

[18] J.A. Xu, E. Huang, J.F. Lin and L.Y. Xu. "Raman Study at High Pressure and the Thermodynamic Properties of Corundum:Application of Kieffer's Model." Am. Miner., vol. 80**,** pp. 1157-1165, 1995.

[19] A. Beran and G.R. Rossman. "OH in Naturally Occurring Corundum." Eur. J. Miner., vol. 18, pp. 441-447, 2006.

[20] F. Jian-Jing, L. Xue-Liang and G. Shou-Guo. The Application of A Mini Raman Spectrometer on

Gemstone Identification and Examination, Translated and prepared by K. Li and K. Carr, B&W Tek Inc., Newark, DE 19713, USA. 2008.

[21] L.E. Cartier. “Ruby and Sapphire from Marosely Madagascar.”J. Gemol., vol. 31, 171-179, 2009.

[22] R. Jacinevicius. Characterization of Vibrational and Electronic Features in the Raman Spectra of Gem Minerals, M.Sc. Dissertation, The University of Arizona, USA., 2009.

[23] S. Achiwawanich, N. Brack, B.D. James and J. Liesegang. “Surface Analysis of Heat Treated Mong Hsu Rubies.”Appl. Surf. Sci., vol. 252, pp. 8646-8650, 2006.

[24] “Bayer Process.”, Internet: http://en.wikipedia.org/wiki/Bayer_process, [Dec. 18, 2015].

[25] A. Rastorguev, M. Baronskiy, A. Zhuzhgov, A. Kostyukov, O. Krivoruchko and V. Snytnikov. “Lowcal Structure of Low-Temperature Υ-Al_2O_3 Phases as Determined by the Luminescence of Cr^{3+} and Fe^{+3}.” RSC Adv., vol. 5, pp. 5686-5694, 2015.

[26] V.C. Farmer Ed., Infrared Spectra of Minerals, Mineralogical Society of London SW7 5HR, 1974.

[27] M. Hatipoglu and M. Akgun. “Zultanite or Color Change from the Milas (Mugla) Region, Turkey” The Austr. Gemol., vol. 23, pp. 481-562, 2009.

[28] M. Hatipoglu, N. Turk, S. C. Chamberlin and A. Akgun. “Gem-Quality Transparent Diaspore (zultanite) in Bauxite Deposits of the Ilbir Mountains, Mendares Massif, SW, Turkey.”Miner. Deposita, vol. 45, pp. 241-245, 2009.

[29] K. Thirangoon. Ruby and Pink Sapphire from Aappaluttoq, Greenland Status of On-going Research, http://www.giathai.net/pdf/Greenland_Ruby_March_2009.pdf, GIA Lab, Bangkok, 2009.

[30] N.I. Leonyuk, A.V. Lyutin, V.V. Maltsev, S.N. Barilo, G.L. Bychko, L.A. Kurnevich, G.A. Emelchenko, V.M. Masalov and A.A. Zhokhov. “Growth and Morphology of Ruby Crystals with Unusual Chromium Concentration.” J. Cryst. Growth., vol. 280, pp.551-556, 2005.

[31] S.A. Basun, R.S. Meltzer and G.F. Imbusch. “Exchange-Coupled Chromium Ion Pairs in Ruby Revisited.”J. Lumin., vol. 125, pp. 31-39, 2007.

[32] D. Schwarz, V. Pardieu, J.M. Saul, K. Schmetzer, B.M. Laurs, G. Giuliani, L. Klemm, A.K. Malsy, E. Erel, C. Hauzenberger, G.D. Toit, A.E. Fallick and D. Ohnenstetter. “Rubies and Sapphires from Winza, Central Tanzania”, Gems. Gemol., vol. 44, pp. 322-347. 2008

[33] F. Zhang, G. Sun, L. Zheng, S. Liu, B. Liu, L. Dong, L. Wang, W. Zhao, X. Liu, G. Yan, L. Tian and Y. Zeng. “Interfacial study and Energy-Band Alignment of Annealed Al_2O_3 Films Prepared by Atomic Layer Deposition on 4H-SiC.”J. Appl. Phys., vol. 113, pp. 044112:1-4, 2013,

[34] M. Eriksson, J. Sainio and J. Lahtinen. "Chromium Deposition on Ordered Alumina Films: An X-ray Photoelectron Spectroscopy Study of the Interaction with Oxygen Transformation."J. Chem. Phys., vol. 116, 3870, 2002.

[35] E. Ünveren, E. Kemnitz, S. Hutton, A. Lippitz and W.E.S Unger. "Analysis of Highly Resolved X-ray Photoelectron Cr 2p Spectra Obtained with a Cr_2O_3 Powder Sample Prepared with Adhesive Tape."Surf. Interface. Anal., vol. 36, pp. 92-95, 2004.

[36] B.P. Payne, M.C. Biesinger and N.S. McIntyre. "X-ray Photoelectron Spectroscopy Studies of Reactions on Chromium Metal and Chromium Oxide Surfaces" J. Electron. Spectrosc. Relat. Phenom., vol. 184, pp. 29-37, 2011.

[37] P. Stefanov, M. Shipochka, P. Stefchev, Z. Raicheva, V. Lazarova and L. Spassov. "XPS Characterization of TiO_2 Layers Deposited on Quartz Plates" J. Phys.: Conference Series, vol. 100, pp. 012039:1-4, 2008.

[38] M.C. Biesinger, L.W.M. Lau, A.R. Gersonb and R.S.C. Smart. "Resolving Surface Chemical States in XPS Analysis of First Row Transition Metals, Oxides and Hydroxides." Appl. Surf. Sci., vol. 257, pp. 887-898, 2010.

[39] T. Hanawa. "A Compressive Review of Techniques for Biofunctionalization of Titanium." J. Periodontal. Implant. Sci., vol. 41, pp. 263-272, 2011.

[40] A.P. Grosvenor, B.A. Kobe, M.C. Biesinger and N.S. McIntyre. "Investigation of Multiplet Splitting of Fe 2p XPS Spectra and Bonding in Iron Compounds." Surf. Interface. Anal., vol. 36, 1564-1574, 2004.

[41] A. Samariya, R.K. Singhal, S. Kumar, Y.T. Xing, M. Alzamora, S.N. Dolia, U.P. Deshpande, T. Shripathi and E.B. Saitovitch. "Defect Induced Reversible Ferromagnetism in Fe-doped ZnO Semiconductor: An Electronic Structure and Magnetization Study."Mater. Chem. Phys., vol. 123, pp. 678-684, 2010.

[42] D. Sethi, A. Pal, R. Sakthive, S. Pandey, T. Dash, T. Das and R. Kumar."Water Disinfection Through Photoactive Modified Titania"J. Photochem. Photobiol. B, vol. 130, pp. 310-317, 2014.

[43] "XPS Reference Page: Oxygen 1s for Organic Compounds",

Internet: http://www.xpsfitting.com/search/label/Oxygen, [Dec. 22, 2015].

[44] A.R. Moon and M.R. Phillips. "Defect Clustering and Colour in Fe,Ti:α Al_2O_3."J. Am.Ceram. Soc., vol. 77, pp. 356-367,1994.

[45] K. Nassau. "The Physics and Chemistry of Colour: The Fifteen Causes of Color", 2nd ed., New York: John Wiley & Sons Inc., 2001.

[46] E. Gaudry, A. Kiratisin, P. Sainctavit, C. Broude, F. Mauri and A. Ramos. "Structural and Electronic

Relaxations Around sSubstitutional Cr^{3+} and Fe^{3+} ions." Phys. Rev. B, vol. 67**,** pp. 094108: (1-10), 2003.

[47] K. Eigenmann, K. Kurtz and H. H. Gunthard. "The Optical Spectrum of Al_2O_3:Fe^{3+}." Chem. Phys. Lett., vol. 13**,** pp. 54-57, 1972.

[48] K. Schmetzer and H. Bank. "The Colour of Natural Corundum." N. Jb. Miner. Mh., vol. 2, pp. 59-68, 1981.